

The Power Spectrum of the Lyman- α Forest at $z < 0.5$

VIKRAM KHAIRE,¹ MICHAEL WALTHER,^{1,2,3} JOSEPH F. HENNAWI,^{1,2} JOSE OÑORBE,⁴ ZARIJA LUKIĆ,⁵
J. XAVIER PROCHASKA,⁶ TODD M. TRIPP,⁷ JOSEPH N. BURCHETT,⁸ AND CHRISTIAN RODRIGUEZ¹

¹*Physics Department, Broida Hall, University of California Santa Barbara, Santa Barbara, CA 93106-9530, USA*

²*Max-Planck-Institut für Astronomie, Königstuhl 17, 69117 Heidelberg, Germany*

³*International Max Planck Research School for Astronomy & Cosmic Physics at the University of Heidelberg*

⁴*Royal Observatories, Blackford Hill, Edinburgh EH9 3HJ, UK*

⁵*Lawrence Berkeley National Laboratory, 1 Cyclotron Road, Berkeley, CA 94720, USA*

⁶*Astronomy and Astrophysics, UC Santa Cruz, 1156 High St., Santa Cruz, CA 95064, USA*

⁷*Department of Astronomy, University of Massachusetts - Amherst, 710 North Pleasant Street, Amherst, MA 01003-9305, USA*

⁸*UCO / Lick Observatory, University of California, Santa Cruz*

Abstract

We present new measurements of the flux power-spectrum $P(k)$ of the $z < 0.5$ H I Lyman- α forest spanning scales $k \sim 0.001 - 0.1 \text{ s km}^{-1}$. These results were derived from 65 far ultraviolet quasar spectra (resolution $R \sim 18,000$) observed with Cosmic Origin Spectrograph (COS) on board Hubble Space Telescope. The analysis required careful masking of all contaminating, coincident absorption from H I and metal-line transitions of the Galactic interstellar medium and intervening absorbers and proper treatment of the complex COS line-spread function. From the $P(k)$ measurements, we estimate the H I photoionization rate (Γ_{HI}) in the $z < 0.5$ intergalactic medium. Our results confirm most of the previous Γ_{HI} estimates based on the H I Lyman- α line-fitting and low- z measurements of $P(k)$. We conclude that previous concerns of a photon underproduction crisis are now resolved by showing that the measured Γ_{HI} is contributed by ultraviolet emission from quasars alone. In a companion paper, we will present constraints on the thermal state of the $z < 0.5$ intergalactic medium from the $P(k)$ measurements presented here.

Keywords: Intergalactic medium — UV background — Lyman- α forest — quasars

1. INTRODUCTION

The intergalactic medium (IGM), being the largest reservoir of the baryons in the Universe, plays an important role in the formation of cosmic structures. The ultraviolet (UV) radiation emanating from this cosmic structure photoionizes and heats the IGM. The trace amount of neutral hydrogen in the highly-ionized IGM imprints a swath of absorption lines on the spectra of background quasars known as the Lyman- α forest. Observations of the Lyman- α forest in a large sample of background quasar sightlines can probe the underlying density fluctuations in the IGM, measure its thermal state, and determine the amplitude of the UV ionizing background.

The temperature and density of the photoionized IGM follow a tight power-law relation over two decades in the density, $T(\Delta) = T_0 \Delta^{\gamma-1}$, where $\Delta = \rho/\bar{\rho}$ is the overdensity, T_0 is the temperature at mean density $\Delta = 1$, and γ is the power-law index. This power-law relation quantifies the thermal state of the IGM (Hui & Gnedin 1997; Theuns et al. 1998; McQuinn 2016). While a wide variety of statistics have been applied to Lyman- α forest spectra with the goal of measuring its thermal state (Haehnelt & Steinmetz 1998; Schaye et al. 1999; Zaldarriaga et al. 2001; McDonald et al. 2006; Lidz et al. 2010; Becker et al. 2011; Bolton et al. 2012; Rorai et al. 2017; Hiss et al. 2017), the power spectrum of the transmitted flux is appealing for several reasons: 1) it is sensitive to a broad range of scales and in particular the small-scales that encode information about thermal state, 2) is thus highly sensitive and capable of breaking strong parameter degeneracies, 3) systematics due to noise, metal-line contamination, resolution effects, and continuum errors

impact it in well-understood ways, and 4) it can be described by a simple multivariate Gaussian likelihood enabling straightforward principled statistical analysis and parameter inference (Irsic et al. 2017a; Walther et al. 2018a,b). For these reasons, the power-spectrum has also been used to constrain other parameters such as the intensity of the UV ionizing background (Gaikwad et al. 2017a), alternate cosmology models with warm and fuzzy dark matter (Viel et al. 2008, 2013; Garzilli et al. 2017; Irsic et al. 2017a), and cosmological parameters including neutrino masses (McDonald et al. 2006; Palanque-Delabrouille et al. 2013, 2015; Yèche et al. 2017; Irsic et al. 2017b).

There are many measurements of the flux power-spectrum at high redshifts (e.g. McDonald et al. 2000; Croft et al. 2002; Kim et al. 2004; Palanque-Delabrouille et al. 2013; Irsic et al. 2017a; Yèche et al. 2017; Walther et al. 2018a) where ground-based telescopes with medium or high resolution spectrographs were used to observe the Lyman- α forest redshifted to optical wavelengths. However to date, there are no measurements at low-redshifts $z < 1.6$ (but see Gaikwad et al. 2017a) where space-based observations are required because the redshifted Lyman- α transition lies in the UV below the atmospheric cutoff. Recently, large surveys (e.g. Tumlinson et al. 2013; Danforth et al. 2016; Burchett et al. 2015; Borthakur et al. 2015) have gathered a significant amount of Lyman- α forest spectra using the Cosmic Origin Spectrograph (COS) on-board the Hubble Space Telescope (HST) that can be used to measure the Lyman- α forest power-spectrum at low redshifts.

The power spectrum at low redshift is of particular interest since it provides another method for measuring the UV ionizing background, whereas previous work based on fitting the distribution of column densities argued for a ‘photon underproduction crisis’ (Kollmeier et al. 2014; Wakker et al. 2015). Perhaps even more interesting is the fact that the power spectrum can measure the thermal state of the low redshift IGM, where long after the impulsive photoheating from reionization events is complete, theory robustly predicts the IGM should have cooled down to temperatures of $T_0 \simeq 5000$ K at $z = 0$ (see e.g. McQuinn 2016; Upton Sanderbeck et al. 2016). Constraints on the low-redshift thermal state would thus provide an important check on our theoretical understanding of the IGM and shed light on the degree to which any other processes such as blazar heating, feedback from galaxy formation, or any other exotic physics can inject heat into the IGM. In an earlier study using the Space Telescope Imaging Spectrograph, Davé & Tripp (2001) obtained preliminary evidence that the

T_0 is indeed about 5000 K at $z \sim 0$, but they also found that the observed low- z Lyman- α lines are not consistent with pure thermal broadening and may therefore also be broadened by some additional processes such as some type of feedback. Similar issues with line broadening are also reported by Gaikwad et al. (2017b); Viel et al. (2017) and Nasir et al. (2017). We can now revisit these issues with much larger sample.

In this paper we present new measurements of the Lyman- α forest flux power spectrum at $z < 0.5$ in five redshift bins. We use high quality Lyman- α forest spectra (S/N per pixel > 10) observed in 65 background quasars from the sample of Danforth et al. (2016). Combining these power spectrum measurements with state of the art cosmological hydrodynamical simulations run with the Nyx code (Almgren et al. 2013; Lukić et al. 2015), we constrain the intensity of UV background Γ_{HI} at $z < 0.5$. Our UV background measurements are consistent with recent studies (Shull et al. 2015; Gaikwad et al. 2017a,b; Fumagalli et al. 2017) which confirm that there is no crisis with UV photon production at $z < 0.5$ and that the primary contributors to the UV background are quasars. In a companion paper (Walther et al. in prep) we will use these power-spectrum measurements to constrain the thermal state of the IGM at $z < 0.5$.

The paper is organized as follows. In Section 2 we discuss the Lyman- α forest data. In Section 3 we describe our method to compute the power spectrum and present the resulting measurements. In Section 4 we discuss the implications of our power spectrum regarding the UV ionizing background and compare with previous work. In Section 5 we present our conclusions and discuss future directions. Throughout the paper we adopt a flat Λ CDM cosmology with parameters $\Omega_m = 0.319181$, $\Omega_b h^2 = 0.022312$, $h = 0.670386$, $n_s = 0.96$, and $\sigma_8 = 0.8288$ consistent with Planck Collaboration et al. (2018). This cosmology is used both for our power spectrum measurements as well as for our cosmological hydrodynamical simulations. All the distances quoted are comoving.

2. DATA AND MASKING

We use high-quality medium-resolution ($R \sim 18000$, $\Delta v \sim 17$ km s $^{-1}$) quasar spectra obtained from HST/COS as a part of the large low- z IGM survey by Danforth et al. (2016). The survey contains 82 quasar spectra at $z_{\text{em}} < 0.72$ observed in the wavelength range from 1130 – 1800, Å which covers the Lyman- α forest at $z < 0.48$. The observations were obtained with grating G130M and G160M from year 2009 to 2013. Danforth et al. (2016) co-added individual spectra (combining

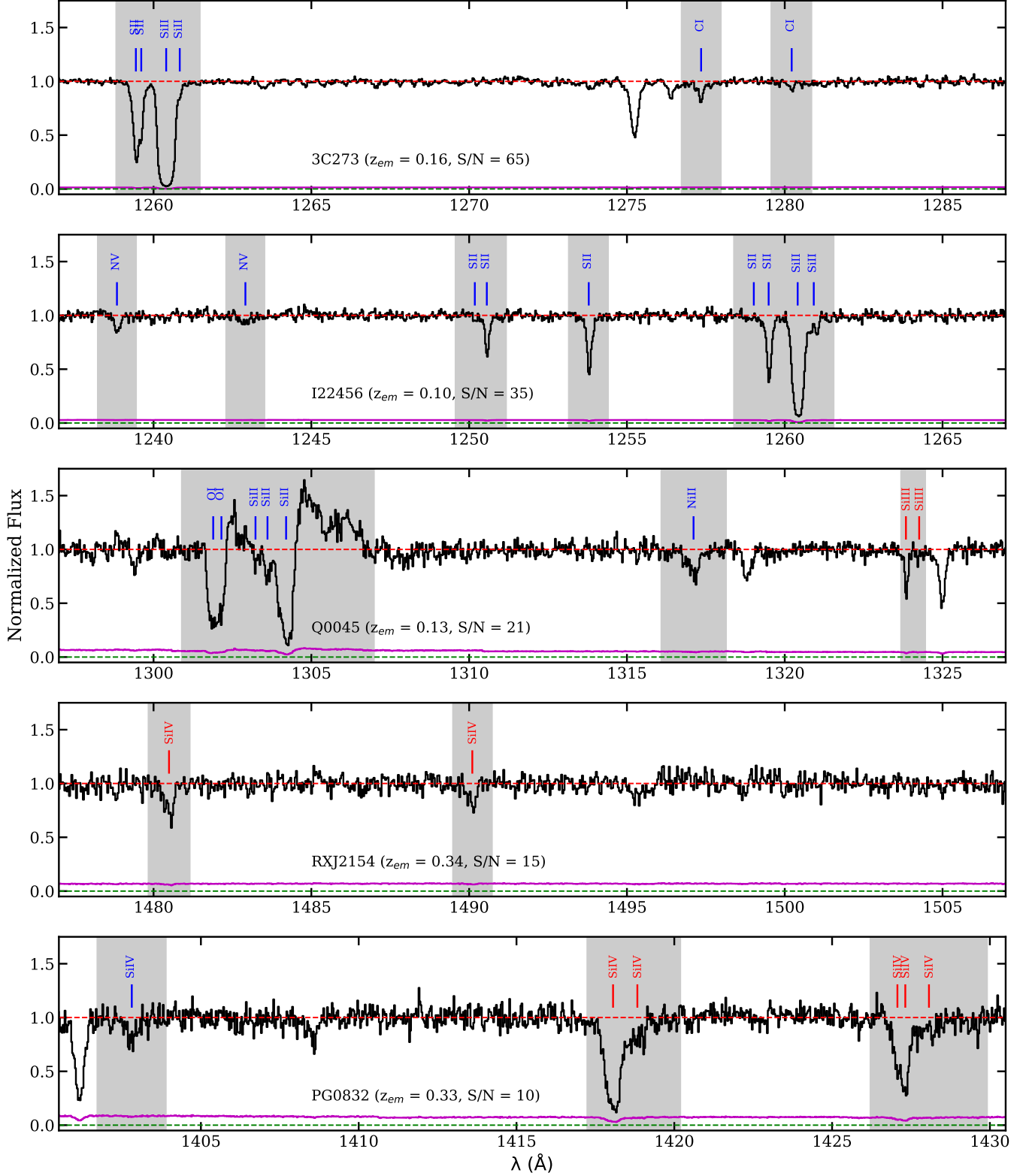


Figure 1. Illustration of our masking procedure. Different panels show random 30 Å chunks of the five quasar spectra with different S/N per pixel as denoted in panels, in decreasing order from top to bottom panel. The red and green dash lines indicate continuum ($y = 1$ line) and zero level ($y = 0$ line). Magenta curve shows the error in the normalized flux. The shaded regions show our masks. Blue and red ticks indicate the metal absorption from the interstellar medium of the Milky Way and from intervening absorbers, respectively. We also mask geocoronal airglow emissions as shown in middle panel associated with O I (at $\lambda \sim 1305$ Å).

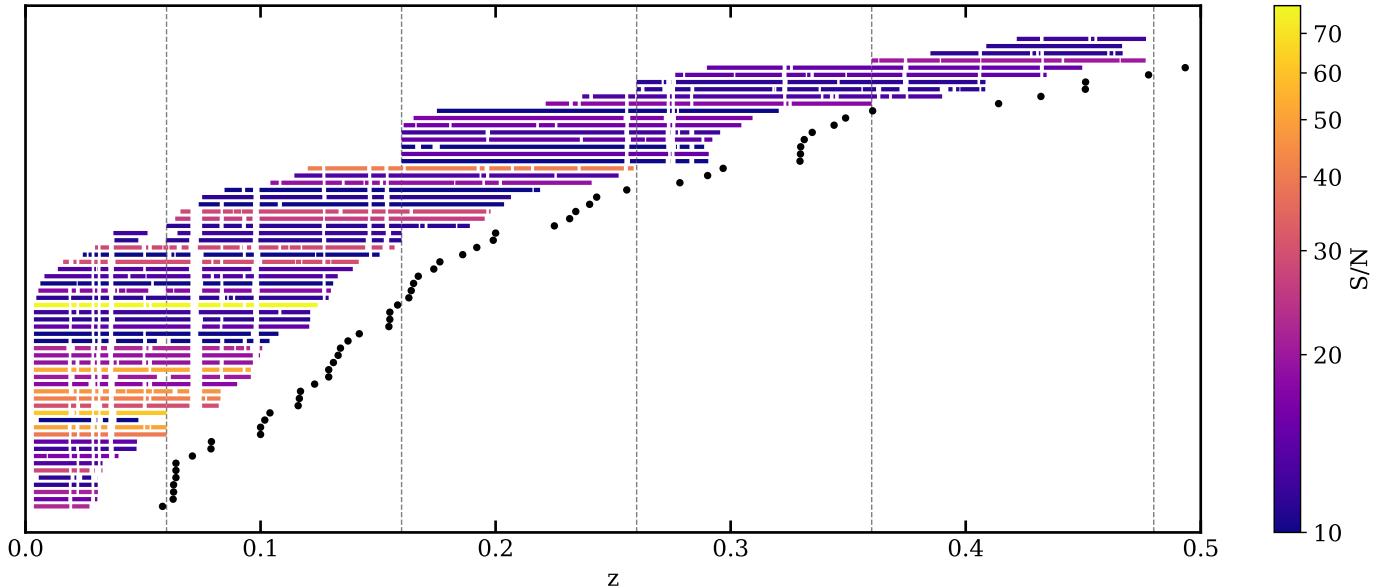


Figure 2. Redshift path covered by the Lyman- α forest used for our power-spectrum calculations. Horizontal lines indicate the Lyman- α redshift path (rest frame 1050 to 1180 Å), filled circles show the emission redshift of quasars, and vertical dashed lines demarcate the redshift bins used (i.e. 0-0.06, 0.06-0.16, 0.16-0.26, 0.26-0.36 and 0.36-0.48). The gaps in the horizontal lines are the masked regions of spectra (see e.g Fig. 1) containing metal lines, emission lines, spectral-gaps, and bad data. This is a subsample of spectra from Danforth et al. (2016) where the unmasked Lyman- α forest has S/N (per COS pixel) ≥ 10 , as indicated with a colorbar.

both gratings whenever available), fitted continua, and identified almost all individual absorption and emission lines. We use these continuum-fitted spectra along with the line catalog made publicly available by Danforth et al. (2016) as a high-level science product at Mikulski Archive for Space Telescope¹.

To calculate the Lyman- α forest flux power spectrum, $P(k)$, we mask all absorption lines arising from higher Lyman series transitions than Lyman- α , the metal lines arising from intervening systems and the interstellar medium of the Milky-way, all emission lines including geocoronal airglow emission, low quality data having $S/N < 5$ per pixel², and all gaps in the spectral coverage. To illustrate our masking procedure, we show five random chunks of spectra with different S/N in Fig 1. The shaded regions in Fig 1 show our masks. This masking is important to remove metal contamination and estimate the power spectrum correctly (see e.g, Walther et al. 2018a). We discuss the effect of not masking metals on the power spectrum in Appendix A.

After masking, we restrict our further analysis to the rest-frame wavelength range between 1050 and 1180 Å in each quasar spectrum to avoid proximity zones of quasars ($\lambda > 1180$ Å) and the excessive masking of

data due to the presence of higher Lyman series forest lines ($\lambda < 1050$ Å). The redshift path covered by the unmasked Lyman- α forest data is shown in Fig. 2 where the quasars are ordered vertically by increasing redshift. Gaps in the horizontal lines show our masking. Vertically aligned gaps indicate masking due to strong Milky-way metal lines. A large gap at 1305 Å ($z \sim 0.7$) is due to a combination of an O I geocoronal airglow emission line and strong Si II and O I absorption lines from the Milky-way (see e.g the middle panel of Fig. 1).

After masking and choosing the relevant wavelength range, we calculate the median S/N per pixel in the unmasked regions and apply a median S/N per pixel > 10 cut to the 82 quasar spectra. Although in our power spectrum calculation we subtract the noise (see Section 3), we choose this S/N cut to make sure that we are not sensitive to systematic errors associated with how well we know the properties of the noise. Note that our S/N estimate is different than the default values provided in Danforth et al. (2016) who computed S/N per resolution element over the entire spectrum. After applying our S/N cut, we are left with the Lyman- α forest of 66 quasars out of the initial 82. Individual values of this S/N per pixel are indicated in Fig 2 via different colors.

We then split the total redshift path covered by these 66 high S/N Lyman- α forest spectra into five redshift bins as illustrated by the vertical dashed lines in Fig. 2

¹ Link: <http://archive.stsci.edu/prepds/igm/>

² A pixel in this dataset corresponds to $\Delta v = 6.67 \text{ km s}^{-1}$.

Table 1. Details of the data and comparison simulation

Redshift bin	\bar{z}^a	Number of quasars	Simulation redshift	Simulation T_0 (K) and γ	
0.005 - 0.06	0.03	39	0.03	5033	1.73
0.06 - 0.16	0.10	34	0.10	5288	1.72
0.16 - 0.26	0.20	19	0.20	5652	1.71
0.26 - 0.36	0.30	13	0.30	6010	1.69
0.36 - 0.48	0.41	9	0.40	6368	1.68

^aMean redshift of the unmasked Lyman- α forest in the bin

and summarized in Table 1. The first bin is chosen from $z = 0.005$ to 0.06 to remove any systematics arising from the extended wings of geocoronal Lyman- α emission line, which sets the lower limit of this redshift bin. The next three bins ($z = 0.06 - 0.16$, $z = 0.16 - 0.26$ and $z = 0.26 - 0.36$) are chosen to have the same width ($\Delta z = 0.1$) and also because the mean redshifts of the Lyman- α forests in these bins are nicely centered at $z = 0.1$, 0.2 , and 0.3 where we can compare our UV background measurements with previous studies (e.g. Shull et al. 2015; Gaikwad et al. 2017a,b). The last redshift bin ($z = 0.36 - 0.48$) encloses the remaining redshift-path covered by the data. Finally, in each redshift bin we removed short spectra that span less than 10% of the redshift bin-width. This criteria removes one more spectrum from the last bin and we are left with a total of 65 quasar spectra shown in Fig. 2.

3. POWER SPECTRUM

In this next section we discuss our method for measuring the power spectrum and present the measurement.

3.1. Method

Once the data are prepared, we calculate the $P(k)$ following the method presented in Walther et al. (2018a). A brief description of the method is as follows. We first calculate the flux contrast of each spectrum in a redshift bin $\delta_F = (F - \bar{F})/\bar{F}$ where \bar{F} is the mean flux of that spectral chunk in the bin. Then we use a Lomb-Scargle periodogram (Lomb 1976; Scargle 1982) to calculate the raw power spectrum $P_{\text{raw}}(k)$. We subtract off the noise power $P_{\text{noise}}(k)$ from $P_{\text{raw}}(k)$ and divide the difference by the square of the window function $W(k, R)$ corresponding to the appropriate COS line spread function (LSF) to correct for finite resolution and pixelization (for more details see Palanque-Delabrouille et al. 2013; Walther et al. 2018a). Therefore, our final power spectrum is

$$P(k) = \left\langle \frac{P_{\text{raw}}(k) - P_{\text{noise}}(k)}{W^2(k, R)} \right\rangle. \quad (1)$$

We use the same logarithmic binning used in Walther et al. (2018a), and the average is performed over individual Lomb-Scargle periodograms of all Lyman- α forest chunks in each bin. We follow the standard normalization of the power spectrum for recent measurements, i.e. the variance in the flux contrast is $\sigma_{\delta_F}^2 = \int_{-\infty}^{\infty} dk P(k)/2\pi$. The noise power is calculated using many realizations of Gaussian random noise³ generated from the error vectors in each spectrum of the bin. For estimating the window function, we used the COS LSFs of different gratings and lifetime positions⁴ depending on the observation setting for each spectrum. The COS LSF is quite different from the typical Gaussian LSFs that govern ground based spectroscopic observations and exhibits broad wings. In Appendix C, we discuss the effect of incorrectly assuming a Gaussian LSF on the obtained $P(k)$ instead of using the correct non-Gaussian COS LSF. Finally, we calculate the uncertainties in $P(k)$, the diagonal elements of covariance matrix $C_{ii} \equiv \sigma_i^2$, by bootstrap resampling using 10^4 random realizations of the dataset. Note that we do not have enough data to estimate the full covariance matrix C_{ij} . We recommend that researchers attempting to fit our power spectrum calculate the full covariance matrix by computing the correlation matrix $R_{ij} = C_{ij}/\sigma_i\sigma_j$ from their models, which can then be scaled by our diagonal elements to determine the full covariance matrix (see e.g. Walther et al. 2018a, for details). Our $P(k)$ measurements and the diagonal elements of covariance matrix are given in Table 2.

3.2. Results

In Fig 3 we show our power spectrum measurement in the different redshift bins, which reliably probes the power over the range $k \sim 5 \times 10^{-4}$ to 0.15 s km^{-1} (see Table 2). In contrast to $z > 2$, the easy identification and masking of metal absorption lines at these low redshifts allows us to probe the small-scale (high- k) power-spectrum with negligible systematics due to non-Lyman- α absorption. We discuss the effect of not masking metals on the power spectrum in Appendix A.

At all redshifts, our measured power spectrum shows a clear small scale cut-off at $k > 0.03 \text{ s km}^{-1}$. This cut-off is a signature of pressure smoothing and Doppler broadening of the Lyman- α forest. At small scales the Lyman- α forest is supported by the thermal-pressure and does

³ Since our S/N cut is ≥ 10 , we are always in the Gaussian regime with sufficient number of photons.

⁴ We use the python package `linetools` (<https://linetools.readthedocs.io/en/latest/api.html>) which can interpolate the COS LSFs from http://www.stsci.edu/hst/cos/performance/spectral_resolution/ to any central wavelength.

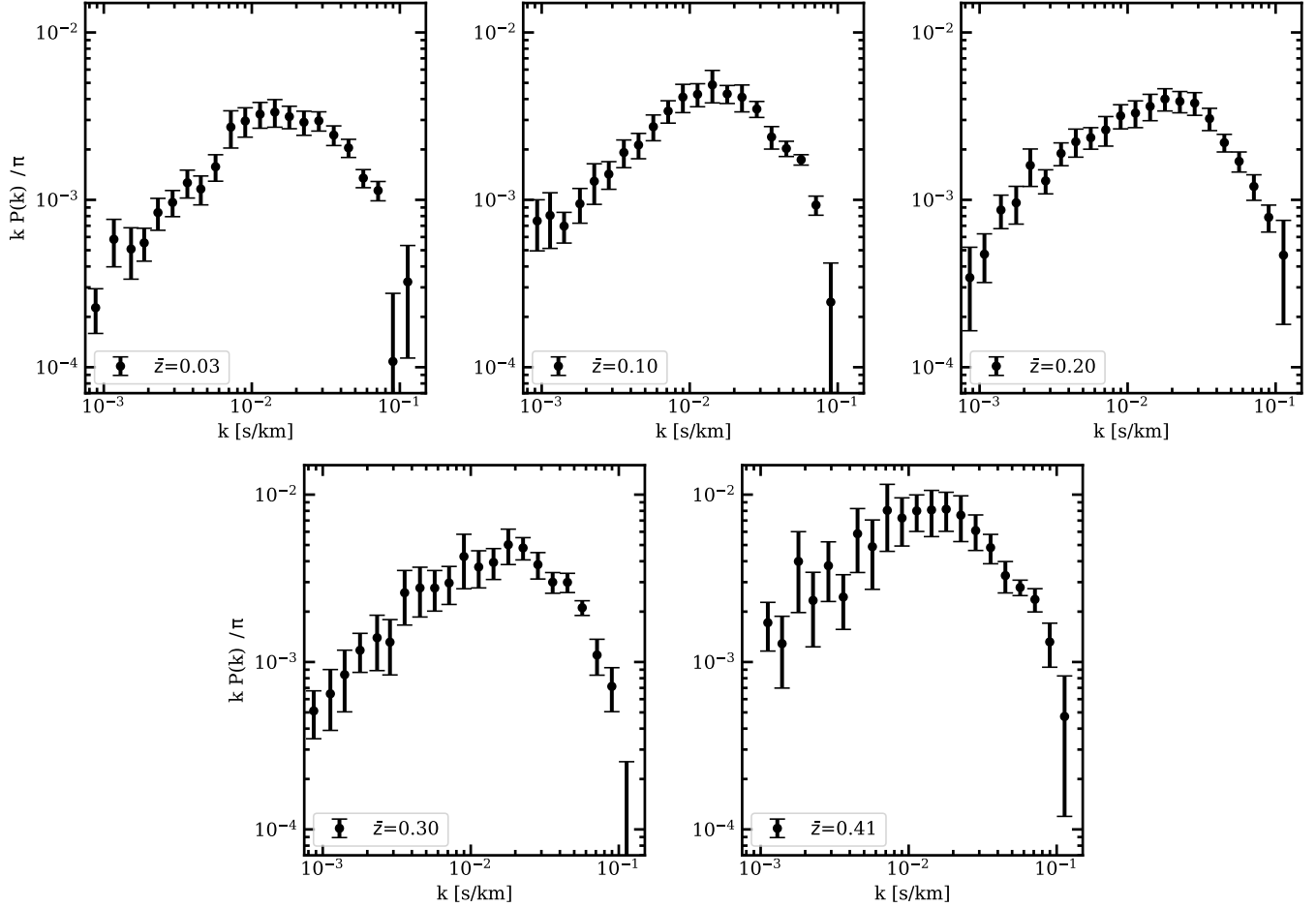


Figure 3. Our Lyman- α forest flux power spectrum (k versus $kP(k)/\pi$) in different redshift bins (see Table 1 for more details) at $k = 8 \times 10^{-4}$ to 0.15 s km^{-1} . The complete measurements are provided in Table 2.

not follow the dark-matter density fluctuations (Hui & Gnedin 1997; Kulkarni et al. 2015; Oñorbe et al. 2017; Rorai et al. 2017). This pressure support, in addition to the Doppler broadening, smooths out the fluctuations in the Lyman- α forest flux and gives rise to the small-scale cut-off seen in the power spectrum (see e.g., Peebles et al. 2010; Rorai et al. 2013). This cut-off is an important feature that probes the thermal state of the IGM (Zaldarriaga et al. 2001; Walther et al. 2018b).

The amplitude of the power spectra at all k is significantly smaller than that obtained at high- z (see, e.g., Walther et al. 2018a). This is because the density evolution of the Universe results in lower overall opacity in the low- z IGM giving rise to a thinner low- z Lyman- α forest. This reduced opacity also reduces the power at all scales. Nevertheless, we obtained high precision measurements (15% at $z < 0.2$, 25% at $z = 0.3$ and 30% at $z = 0.41$ over $0.001 < k < 0.1 \text{ s km}^{-1}$ scale) of the power spectrum because of the large sample size. In contrast to high- z , the redshift evolution of the amplitude of the power appears quite shallow. This evo-

lution is so weak that it is challenging to identify it, for example our large scale power ($k < 0.02 \text{ s km}^{-1}$) measurement at $\bar{z} = 0.2$ is only slightly lower than at $\bar{z} = 0.1$. Such non-monotonic redshift evolution is unexpected, but likely results from a combination of noise fluctuations and very shallow redshift evolution. Indeed, extremely shallow evolution of the power spectrum amplitude is not unexpected at low- z . The power spectrum $P(k, z) \propto \langle FF^* \rangle \propto e^{-2\tau(z)}$ scales with the evolution of the optical depth $\tau(z)$. Following the fluctuating Gunn-Peterson approximation (FGPA), we can write (Gunn & Peterson 1965; Croft et al. 1998)

$$\tau(z) \propto \Gamma_{\text{HI}}^{-1} T_0^{-0.7} n_{\text{H}}^2, \quad (2)$$

where Γ_{HI} is the photoionization rate of H I from the UV background (UVB) and n_{H} is the hydrogen density. Using $\Gamma_{\text{HI}}(z) \propto (1+z)^5$ (from Shull et al. 2015; Gaikwad et al. 2017a), $n_{\text{H}}(z) \propto (1+z)^3$ from cosmological density evolution, and assuming a power law redshift evolution for $T_0(z) \propto (1+z)^\beta$, the opacity of the IGM should scale as $\tau \propto (1+z)^{1-0.7\beta}$. In the absence of

any non-standard heating processes, theory predicts a cool-down of the IGM at low redshift suggesting $\beta > 0$. This suggests that $\tau(z)$ and the resulting amplitude of the power spectrum evolve slowly at low redshifts. However, note that the FGPA is not a good approximation for the low- z IGM, at least for the power spectrum at large scales (small k), because it does not include the effects of shock-heated gas, as explained in Section 4 and Fig. 4. Therefore, the redshift evolution of the amplitude of the large scale power is likely to be more complicated than the simple picture presented here.

The flux power spectrum at redshifts $0.1 \leq z \leq 0.4$ was also presented by Gaikwad et al. (2017a), however they split observed spectra into chunks of size 50 cMpc/h to compare with their simulation box size for the specific purpose of only evaluating the UV background. Also their method of calculating the power spectrum and the normalization is quite different from ours. For example, they fill the masks with continuum added random noise and estimate the power spectrum of the flux (f) rather than the flux-contrast (δf). For these reasons, we are unable to compare with the Gaikwad et al. (2017a) power spectrum measurements. However, we can compare with their UV background measurements which not only use the power-spectrum but also the flux probability density function (PDF) and column-density distribution function (CDDF; Gaikwad et al. 2017b).

4. IMPLICATIONS FOR THE UV BACKGROUND

The amplitude of the Lyman- α forest power spectrum is sensitive to the UV background, therefore it can be used to measure the UV background quantified by the H I photoionization rate Γ_{HI} . The basic idea behind the measurement is to compare the power-spectrum with cosmological hydrodynamical simulations of the IGM where Γ_{HI} is one of the free parameters. In this section, we first discuss our IGM simulations and then the Γ_{HI} measurements obtained from them.

4.1. Simulations

For comparing our power spectrum measurements with the simulated IGM, we ran Nyx cosmological hydrodynamic simulation (Almgren et al. 2013; Lukić et al. 2015) from $z = 159$ to $z = 0.03$. This is a grid-based Eulerian hydrodynamic simulation of box size 20 cMpc/h and 1024^3 cells. The simulations resolve 19.5 ckpc/h scales (i.e, $\Delta v < 2$ km/s at $z < 0.5$). The initial conditions were generated using transfer function and the Zel'dovich (1970) approximation. We evolve baryon hydrodynamics in Eulerian approach on a fixed Cartesian grid with 1024^3 cells, and follow the evolution of dark

Table 2. Power spectrum measurement ^a

\bar{z}	$k(s/km)$	$kP(k)/\pi$	$\sigma_{kP(k)}/\pi$
0.03	3.937×10^{-4}	1.874×10^{-4}	7.550×10^{-5}
0.03	4.390×10^{-4}	1.228×10^{-4}	5.164×10^{-5}
0.03	7.825×10^{-4}	3.137×10^{-4}	9.136×10^{-5}
0.03	8.805×10^{-4}	2.267×10^{-4}	6.759×10^{-5}
0.03	1.170×10^{-3}	5.812×10^{-4}	1.833×10^{-4}
0.03	1.528×10^{-3}	5.083×10^{-4}	1.726×10^{-4}
0.03	1.874×10^{-3}	5.534×10^{-4}	1.232×10^{-4}
0.03	2.322×10^{-3}	8.393×10^{-4}	1.814×10^{-4}
0.03	2.915×10^{-3}	9.651×10^{-4}	1.717×10^{-4}
0.03	3.670×10^{-3}	1.265×10^{-3}	2.399×10^{-4}
0.03	4.523×10^{-3}	1.161×10^{-3}	2.277×10^{-4}
0.03	5.691×10^{-3}	1.576×10^{-3}	2.837×10^{-4}
0.03	7.217×10^{-3}	2.721×10^{-3}	6.823×10^{-4}
0.03	9.028×10^{-3}	2.958×10^{-3}	5.895×10^{-4}
0.03	1.137×10^{-2}	3.248×10^{-3}	5.704×10^{-4}
0.03	1.431×10^{-2}	3.343×10^{-3}	6.273×10^{-4}
0.03	1.792×10^{-2}	3.142×10^{-3}	4.820×10^{-4}
0.03	2.250×10^{-2}	2.907×10^{-3}	4.776×10^{-4}
0.03	2.837×10^{-2}	2.966×10^{-3}	3.903×10^{-4}
0.03	3.578×10^{-2}	2.438×10^{-3}	3.273×10^{-4}
0.03	4.503×10^{-2}	2.045×10^{-3}	2.542×10^{-4}
0.03	5.666×10^{-2}	1.349×10^{-3}	1.670×10^{-4}
0.03	7.133×10^{-2}	1.137×10^{-3}	1.502×10^{-4}
0.03	1.131×10^{-1}	3.235×10^{-4}	2.101×10^{-4}

^aThe full table will be available online with the electronic edition of the journal

matter using 1024^3 Lagrangian (N-body) particles. In this simulation, we used the photoheating rates from the Puchwein et al. (2018) non-equilibrium models. We stored simulation outputs at different redshifts corresponding to our \bar{z} at the measured $P(k)$. We determined T_0 and γ by fitting the distribution of densities and temperatures in the simulation following the linear least squares method described in Lukić et al. (2015). The simulation redshifts, T_0 , and γ are provided in Table 1. The values of T_0 and γ are also consistent with the theoretical models presented in McQuinn (2016) and obtained in the simulations presented in Shull et al. (2015) and Gaikwad et al. (2017a).

For our current purposes, the only free parameter in these simulations is Γ_{HI} . We vary Γ_{HI} and generate the simulated Lyman- α forest as follows. First, we calculate the ionization fractions of hydrogen and helium under the assumption of ionization equilibrium including both photoionization and collisional ionization. For this we have used updated cross-sections and recombination rates from Lukić et al. (2015). Then, we extract

a large number (5×10^4) of random lines-of-sight (skewers) parallel to the (arbitrarily chosen) z -axis of the simulation cube. Along these lines-of-sight, we store the ionization fractions, densities, and z -component of the velocities. As our procedure does not include radiative transfer, we model the self-shielding of dense cells using the prescription described in Rahmati et al. (2013). We generate the simulated Lyman- α optical depth for each cell along the line of sight, which we will refer to as τ -skewers, by summing all the real space contributions to the redshift space optical depth using the full Voigt profile resulting from each (real-space) cell following the approximations used in Tepper-García (2006). The flux $F = -\ln \tau$ gives us the continuum normalized Lyman- α forest flux along these skewers. These constitute our ‘perfect-skewers’ from the simulation. We calculate and store 5×10^4 simulated skewers from each box for different values of Γ_{HI} .

Note that every-time we change the Γ_{HI} we recalculate the skewers following the procedure described above. We do not simply rescale the τ values along the skewers when we change the Γ_{HI} , as is typically applied to simulations of the Lyman- α forest at higher redshifts following the FGPA. According to FGPA, $\tau \propto \Gamma_{\text{HI}}^{-1}$ (from Eq 2), which is a good approximation at high- z when most of the gas in the IGM is photoionized. However, a large amount of gas in the low- z Universe is collisionally ionized because it is heated to $T > 10^5$ K by structure formation shocks (see Davé et al. 2010; Shull et al. 2012). In this regime the simple rescaling of τ following FGPA leads to erroneous results, because the contribution of collisional ionization implies that the true optical depth is no longer linearly proportional to Γ_{HI} (see also Lukić et al. 2015). This is illustrated in Fig. 4 where we show the power-spectrum for τ -skewers generated with a fiducial value of $\Gamma_{\text{HI,Fid}} = 1.75 \times 10^{-13} \text{ s}^{-1}$ (black-curve) and three more power-spectra where the τ -skewers were initially calculated for $\Gamma_{\text{HI,Fid}} \times 4$, $\Gamma_{\text{HI,Fid}}/3.5$ and $\Gamma_{\text{HI,Fid}}/2$ values and then rescaled to get the τ -skewers corresponding to $\Gamma_{\text{HI,Fid}}$ following FGPA. The latter three deviate significantly from the fiducial power-spectrum on large scales (low $k < 0.04 \text{ s km}^{-1}$ values). The bottom panel of Fig. 4 shows the percentage differences in the correct calculation versus the ones obtained by using the FGPA. The differences are large (of the order of 10 to 25%) when the FGPA is applied for larger difference in Γ_{HI} (of factor 2 to 4). Given that the reported low- z Γ_{HI} measurements vary over factors of 2 – 5, the results obtained by incorrectly using FGPA can give large systematic differences in the derived Γ_{HI} values.

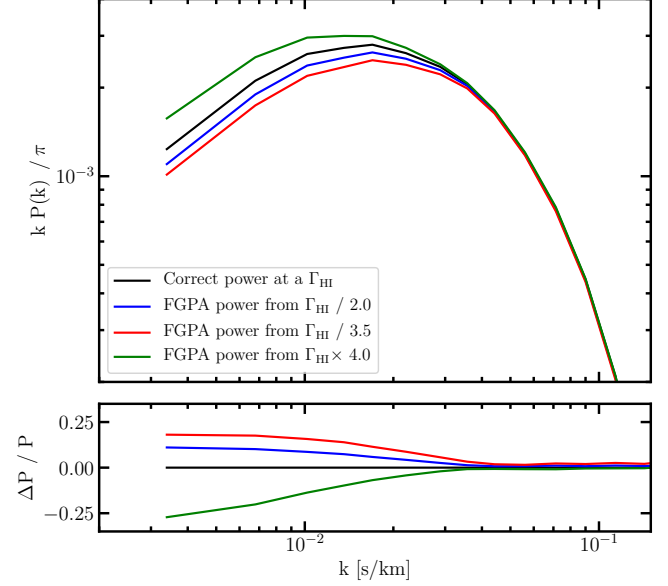


Figure 4. The effect of using FGPA on power-spectra. Top panel shows $z = 0.2$ power-spectrum estimated for $\Gamma_{\text{HI,Fid}} = 1.75 \times 10^{-13} \text{ s}^{-1}$ (black-curve) by correctly calculating the τ -skewers. The green, blue and red curves show power-spectra estimated when τ -skewers, which were initially calculated for $\Gamma_{\text{HI,Fid}} \times 4$, $\Gamma_{\text{HI}}/2$ and $\Gamma_{\text{HI,Fid}}/3.5$ values, were rescaled to $\Gamma_{\text{HI,Fid}}$ values by following FGPA. At $k < 0.04 \text{ s km}^{-1}$ the power-spectra obtained using FGPA deviates from correct power-spectrum (black-curve) and the percentage deviation are shown in the bottom panel with the same colors. The deviation is large for large differences in the initial and final Γ_{HI} values.

Once the perfect-skewers are constructed, we adopt a forward modeling approach to make them look like realistic spectra. To this end we follow the procedure developed in Walther et al. (2018a) but for the HST COS data. We first stitch randomly drawn skewers together to cover the Lyman- α forest redshift path of each quasar. Then we convolve these skewers with the finite COS LSF following different gratings and lifetime position exactly the same as in the data for each quasar. Then we rebin these to match the pixels of the actual data. After that, we add Gaussian random noise at each pixel generated with the standard deviation of the error-vector from the observed spectra. Then we mask these spectra in the exactly same way as the data and follow the same procedure to calculate the power-spectrum (see Section 3.1). We calculate $P(k)$ from these forward models created for large number of Γ_{HI} values and estimate the Γ_{HI} by comparing with the $P(k)$ measurements as explained in the next sub-section.

4.2. Constraints on the UV background

The power spectrum is not only sensitive to Γ_{HI} but also to the thermal state of the IGM quantified by T_0 and γ . Therefore, to correctly measure the Γ_{HI} using our power spectrum, we need a large ensemble of simulations of different IGM thermal state models similar to the THERMAL grid⁵ (Hiss et al. 2017; Walther et al. 2018b). We have such a grid with 50 Nyx simulations (with box size 20cMpc/h and 1024^3 particles) of different IGM thermal models at a single redshift $z = 0.2$ overlapping with our dataset. We use these simulations and follow the Bayesian inference approach presented in Walther et al. (2018b) where the likelihood of the model is given by

$$\begin{aligned} \mathcal{L} &\equiv P(\text{data}|\text{model}) \\ &\propto \prod_{\text{datasets}} \frac{1}{\sqrt{\det(C)}} \exp\left(-\frac{\Delta^T C^{-1} \Delta}{2}\right) \\ \Delta &= \mathbf{P}_{\text{data}} - \mathbf{P}_{\text{model}} \end{aligned} \quad (3)$$

Here C is the covariance of the measurements where the diagonal elements are taken from the uncertainties obtained here (see Table 2) and the off-diagonal elements are estimated from the forward model closest in the parameter space to the model in question. Using this \mathcal{L} , we perform a Bayesian inference at $z = 0.2$ using Markov Chain Monte Carlo methods (MCMC) and jointly estimate the T_0 , γ , and Γ_{HI} at $z = 0.2$ (Walther et al in prep.). Then we marginalize the joint posterior distribution over parameters T_0 and γ to determine Γ_{HI} and its 68% confidence interval.

At other redshifts, we do not have such a large simulation grid yet. However the analysis at $z = 0.2$ gives us a clear idea on how much the degeneracies in the thermal state of the low- z IGM propagate into uncertainties on the Γ_{HI} measurements. To estimate the Γ_{HI} at other redshifts but using only one thermal model rather than a large grid of thermal models, we simply assume that the scaling between uncertainties at these redshifts behave similarly to our $z = 0.2$ Γ_{HI} measurement. To quantify the amount by which the uncertainties on the Γ_{HI} can be underestimated if one uses only one simulation instead of the full grid, we repeat the analysis mentioned above at $z = 0.2$ but using only one simulation with Γ_{HI} being the only free parameter. In this analysis, we are using the same simulation for which we have stored outputs at other redshifts as well (as described in section 3 and Table 1). Also, for this Γ_{HI} estimate we opt to use only the diagonal elements of the covariance matrix because the shape of power spectrum is not very flexible in this single parameter model where the IGM

Table 3. Γ_{HI} measurements

\bar{z}	Γ_{HI} (10^{-13} s^{-1})
0.03	$0.585^{+0.17}_{-0.18}$
0.10	$0.756^{+0.17}_{-0.18}$
0.20	$1.135^{+0.32}_{-0.32}$
0.30	$1.479^{+0.44}_{-0.52}$
0.41	$1.418^{+0.53}_{-0.57}$

thermal state is fixed. We found that fitting with the full covariance led to spurious bad fits resulting from the rigidity of the model of the power spectrum shape if the thermal state is fixed. In this case, where we use only one simulation (and hence one thermal model) and the diagonal elements of covariances, we calculate the Γ_{HI} and uncertainties represented by 68% confidence interval on it by performing a maximum likelihood analysis. We find that these uncertainties are underestimated by a factor of 5.75 as compared to the one obtained using full simulation grid and covariances.

We repeat this at other redshifts and obtain the Γ_{HI} and the 68% confidence interval using only diagonal elements. Next, we multiply this confidence interval by factor 5.75 so that it correctly represents the uncertainties arising from degeneracies in the thermal state of the low- z IGM. We believe that this approach of getting uncertainties at redshifts other than $z = 0.2$, although approximate, is nevertheless a significant improvement over previous estimates of Γ_{HI} which are based on IGM simulation output, and thus effectively assume perfect knowledge of the thermal state of the IGM. Nevertheless, in a companion paper (Walther et al in prep.) we will be presenting joint constraints on T_0 , γ , and Γ_{HI} . For all the Γ_{HI} estimates discussed here we have fit our power spectrum measurements over the range $0.03 < k < 0.1 \text{ s km}^{-1}$, where the lowest k is chosen to match our simulation cube size of 20 cMpc/h and highest k where we have reliable uncertainties on the power spectrum measurements. However, note that our results are not sensitive to the choice of lowest k value (k_{min}) as long as it is $0.03 > k_{\text{min}} > 0.01 \text{ s km}^{-1}$.

Our Γ_{HI} measurements and the 68% confidence interval on them obtained following the method mentioned above are provided in Table 3 and shown in Fig. 5. We also show the previous measurements reported in the literature at $z < 0.5$ for comparison (however, see Davé & Tripp 2001, for an early attempt). The upper limit at $z \sim 0$ by Fumagalli et al. (2017) was obtained from the H α and 21-cm observations of a nearby galaxy. All other measurements have used the Lyman- α forest from Danforth et al. (2016). The measurement by Kollmeier et al. (2014) at $z \sim 0.1$ and the fit resulting from the

⁵ Link: <http://thermal.joseonorbe.com/>

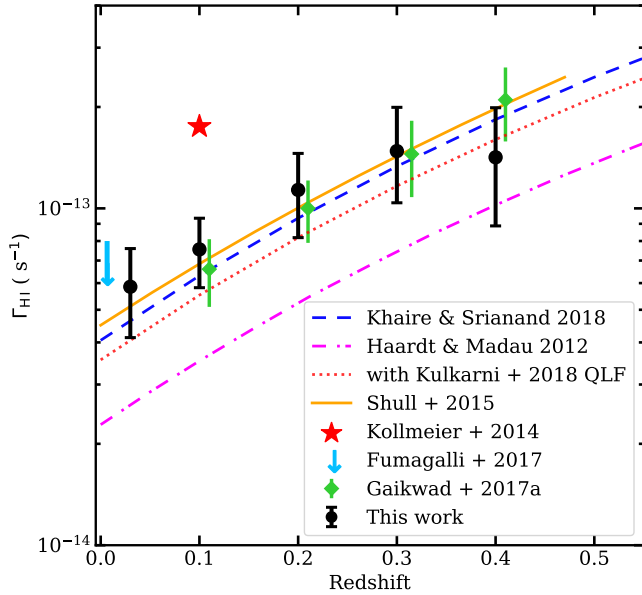


Figure 5. Our estimated Γ_{HI} values (black circles) compared with previous measurements by Gaikwad et al. (2017a, green diamonds), Kollmeier et al. (2014, red star) a fitting form by Shull et al. (2015, orange curve) and upper limits from Fumagalli et al. (2017, downward arrow). Prediction from a new UV background model of Khaire & Srianand (2018, blue-dash curve) is consistent with our measurements. Also the UV background predictions using updated QLF from Kulkarni et al. (2018, red dotted curve) gives consistent results with the measurements (see Section 4.2 for more details). The UV background from Haardt & Madau (2012, magenta dot-dash curve) is factor of ~ 2 smaller than the measurements.

analysis by (Shull et al. 2015) at $z < 0.5$ were obtained by modeling the CDDF, whereas measurements of Gaikwad et al. (2017a) were obtained using flux PDF and power-spectrum (and later confirmed with the CDDF in Gaikwad et al. 2017b). Our measurements are consistent with the previous studies except for Kollmeier et al. (2014), which is ~ 2.5 times higher. As compared to previous studies, we have independent measurements obtained only from the Lyman- α forest power spectrum extending down to $z = 0.03$.

In Fig. 5 we also show predictions from the UV background models by Haardt & Madau (2012) and Khaire & Srianand (2018)⁶. Our Γ_{HI} measurements and also other measurements (except for Kollmeier et al. 2014) are consistent with the Khaire & Srianand (2018) UV background and factor of ~ 2 higher than Haardt & Madau (2012). The Khaire & Srianand (2018) UV back-

ground at $z < 0.5$ is mostly contributed by quasars since it has been obtained with a negligible contribution from galaxies (at $z < 2$; see their Eq. 13). Therefore quasar emission is sufficient to produce the low- z UV background. The factor of five discrepancy between measurement from Kollmeier et al. (2014) and the prediction from Haardt & Madau (2012) was argued to represent a photon-underproduction crisis at low- z . Soon after the Kollmeier et al. (2014) study, Khaire & Srianand (2015a) showed that the UV background models which include an updated quasar emissivity predict a factor of two higher Γ_{HI} , without requiring any additional contribution from galaxies. This model later turned out to be consistent with many new Γ_{HI} measurements (Shull et al. 2015; Gaikwad et al. 2017a,b; Gurvich et al. 2017; Viel et al. 2017; Fumagalli et al. 2017). As shown in Fig 5, this is also consistent with our new measurements. Other recent updates to UV background models (Madau & Haardt 2015; Puchwein et al. 2018; Khaire & Srianand 2018) also came to the same conclusion using more recent estimates for the quasar emissivity similar to Khaire & Srianand (2015a).

Recently, Kulkarni et al. (2018) updated the fits to the quasar luminosity functions (QLF) and emissivity across a large redshift range and claim that the quasar contribution to low- z UV background is factor of ~ 2 smaller than the predictions by these recent UV background models (Khaire & Srianand 2018; Puchwein et al. 2018; Madau & Haardt 2015) and most of the measurements. However, the Kulkarni et al. (2018) calculation uses the CDDF of the IGM from tabulated fits by Haardt & Madau (2012) and an ionizing spectral slope of quasars $f_\nu \propto \nu^{-1.7}$ (Lusso et al. 2015). Instead, using the Inoue et al. (2014) CDDF results in a 40-60% higher UV background at $z < 0.5$ (see for e.g. Figure 16 of Gaikwad et al. 2017a). This along with including the recombination emissivities in the UV background calculations should easily increase the Γ_{HI} estimates of Kulkarni et al. (2018) by factor of ~ 1.8 as shown in Fig. 5. For this calculation we used the UV background code presented in Khaire & Srianand (2018) but with the updated quasar emissivity determined by Kulkarni et al. (2018), with the same limiting magnitude at 1450 \AA ($M_{1450, \text{lim}} = -18$) and the same spectral slope $f_\nu \propto \nu^{-1.7}$ that they adopted, but using the Inoue et al. (2014) CDDF instead of the Haardt & Madau (2012) fits used by Kulkarni et al. (2018). We note that adopting a flatter spectral slope for quasars can further increase the Γ_{HI} . For example redoing the calculation mentioned above using the Kulkarni et al. (2018) emissivity and the Khaire & Srianand (2018) UV background model, but changing the quasar spectra slope to $f_\nu \propto \nu^{-1.4}$ con-

⁶ We use the fiducial Q18 model with spectral slope of quasar $f_\nu \propto \nu^{-1.8}$ at hydrogen ionizing energies (following Lusso et al. 2015; Khaire 2017).

sistent with the harder slope measured by Shull et al. (2012); Stevans et al. (2014) results in a further increase of the Γ_{HI} by a factor of 1.3.

Finally, note that even if the Γ_{HI} is as high as purported by Kollmeier et al. (2014) there is no crisis associated with photon production since a negligible contribution from galaxies, obtained using updated cosmic star formation histories (Madau & Dickinson 2014; Khaire & Srianand 2015b), can easily reproduce it (see for more details Khaire & Srianand 2015a).

5. SUMMARY AND CONCLUSIONS

We present a new high precision high resolution power spectrum measurement in five different redshift bins at $z < 0.5$. For that we have used high-quality medium resolution Lyman- α forest data from HST/COS from the largest low- z IGM survey published by Danforth et al. (2016). We used the procedure developed in Walther et al. (2018a), which takes into account the masks and noise in the data and the finite resolution of the instrument. The data allows us to reliably probe the power spectrum up to small scales $k < 0.1$ s/km and our measurements show the expected thermal cut-off in the power at small scales $k > 0.02$ s/km, resulting from pressure smoothing of IGM gas and thermal Doppler broadening of absorption lines. Our power spectrum measurements are provided in Table 2.

We compare these with cosmological hydrodynamical simulations and obtain constraints of the UV background at $z < 0.5$. Our measured hydrogen photoionization rates (Table 3) are consistent with the previous estimates (Shull et al. 2015; Gaikwad et al. 2017a,b; Fumagalli et al. 2017) and new UV background models (Puchwein et al. 2018; Khaire & Srianand 2018). This suggests that the low- z UV background is dominated by ionizing photons emitted by quasars without requiring any significant contribution from galaxies.

The power-spectrum measurements presented here can probe the thermal state of the low- z IGM. At low- z , theoretical calculations using standard heating and cooling rates show that the IGM loses memory of the previous heating episodes caused by the hydrogen and helium reionization. This makes understanding and predicting the structure of the low- z IGM relatively simple, as it is independent of the physics associated with hydrogen and helium reionization heating which complicates modeling it at higher redshifts $z \gtrsim 2$. In the absence of any other heating processes, theory predicts that the diffuse low-density photoionized IGM cools down after $z < 2$ and asymptotes toward a single temperature-density relation with γ close to 1.6 and $T_0 \sim 5000$ K (McQuinn 2016) at $z = 0$. Such a predicted cool-down of the IGM

at low- z has not yet been observationally confirmed. Indeed there are no reliable measurements of thermal state of the IGM at $z < 1.6$ (but see Ricotti & Shull 2000) where the atmospheric cut-off does not allow us to observe Lyman- α forest from ground based telescopes.

In a companion paper (Walther et al, in prep) we will use the power spectrum measurements presented here to jointly constrain the IGM thermal state (T_0 , γ) and the UV background (Γ_{HI}). These measurements will help us understand the physics of IGM and address important questions such as whether feedback processes associated with galaxy formation modify the thermal state of the IGM at low- z (Viel et al. 2017; Nasir et al. 2017), and/or if there is any room for the existence of non-standard heating processes powered by TeV Blazars (Puchwein et al. 2012; Lamberts et al. 2015) or decaying dark matter (Furlanetto et al. 2006; Araya & Padilla 2014).

In contrast with high- z , the much lower opacity of Lyman series absorption arising in the low- z IGM results in dramatically reduced line blanketing, making it relatively straightforward to identify all lines as either resulting from the Lyman-series or metal absorption. This results in a large redshift path length where Lyman series absorption can be studied, simplifies data analysis and preparation, and mitigates important systematics from metal-line contamination arising at small-scales (high- k ; see section 4.1 of Walther et al. 2018a). Furthermore, our measurements demonstrate that COS resolution is sufficient to obtain high-quality power-spectrum measurements even at small-scales (high- k , $k \sim 0.1$ s km $^{-1}$) required for probing the thermal state of the IGM and demonstrate the important role that HST/UV spectroscopy can play in our understanding of the low- z IGM. We conclude by noting that, owing to the paucity of archival near-UV spectra covering the Lyman- α transition at $0.5 < z < 1.6$, there are essentially no constraints on the physical state of IGM gas in this redshift interval, representing 5 Gyr of the Universe's history. It is critical that HST UV spectroscopy fill this gap in our understanding of the Universe before HST's mission is complete, otherwise we could remain in the dark for decades.

VK thanks R. Srianand, T. R. Choudhury and P. Gaikwad for insightful discussion on the power spectrum normalization. We thank all members of the ENIGMA group⁷ at University of California Santa Barbara for useful discussions and suggestions.

⁷ <http://enigma.physics.ucsb.edu/>

Calculations presented in this paper used the draco and hydra clusters of the Max Planck Computing and Data Facility, a center of the Max Planck Society in Garching (Germany). We have also used the National Energy Research Scientific Computing Center (NERSC)

supported by the U.S. Department of Energy (DoE) under Contract No. DE-AC02-05CH11231.

ZL was in part supported by the Scientific Discovery through Advanced Computing (SciDAC) program funded by the DoE, the Office of High Energy Physics and the Office of Advanced Scientific Computing Research.

APPENDIX

A. POWER SPECTRUM WITHOUT MASKING METAL ABSORPTION LINES

While preparing data for the power spectrum calculation, we have properly masked the metal lines and other contaminations (see Section 2). This is an important procedure to correctly calculate the power spectrum. However, to estimate the relevance of metal contamination, we also calculate the power spectrum without masking metal absorption lines in the Lyman- α forest. However, note that we mask the spectral gaps and all other emission lines, which appear mainly in our lowest redshift bin. In Fig 6, we show the power spectrum calculated for this case along with our fiducial power spectrum measurements. As expected, when metal lines are not masked the power is systematically higher because of the extra fluctuations in the flux introduced by metal lines. However the difference in power is larger at lower redshift mostly because of strong metal contamination arising from the ISM of the Milky-way and many of the absorption lines are correlated as they originate from the same source and with same wavelength separation.

B. EFFECT OF MASKING ON THE POWER-SPECTRUM

To check if the spectral masking is introducing any significant contamination in the power-spectrum we calculate the power spectrum from our forward models (using Γ_{HI} values consistent with our measurements) but without using any masking on the Lyman- α forest. In these forward models for the purpose of only studying the effect of masking, we are using infinite resolution noiseless spectra. In Fig. 7 we compare the resulting power spectrum with and without masking the Lyman- α forest. The bottom panel shows a fractional difference between those. The maximum change in relevant $k < 0.1 \text{ s km}^{-1}$ values is not more than 5% at any redshift. For comparing with the actual uncertainties in the power spectrum, we also plot the fractional errors in the bottom panel. The figure clearly shows that the fractional change in the power-spectrum because of masking is less than the errors on the actual power spectrum measurements. This motivates us not to perform the masking corrections on the measurements as done in Walther et al. (2018a).

C. EFFECT OF COS LSF ON THE POWER-SPECTRUM

The COS LSF is quite different from a Gaussian as it exhibits strong non-Gaussian wings. In the power spectrum calculation the LSF appears in the window function correction (see Eq. 1) and it is also important to generate the forwards models. To see how much the power spectrum can be affected if one uses a Gaussian LSF with similar resolution of COS we perform the following analysis. We use mock spectra generated from our forward models (at Γ_{HI} values consistent with our measurements) generated using the correct COS LSF but while calculating the power spectrum we use a Gaussian LSF. The resulting power spectrum (red-curves) is shown in the Fig 8 along with the one obtained by using the correct COS LSF (black-curves). The amplitude of the power spectrum in the former is smaller at large k values and the differences, as shown in the bottom panels, can be as high as 80%. This is way to large as compared to the actual uncertainties from our measurements. Although the differences decrease at higher redshifts, because of small sample sizes, the discrepancy is too significant to ignore. This exercise shows that it is never a good choice to approximate COS LSF as a Gaussian.

REFERENCES

- | | |
|--|--|
| <p>Almgren, A. S., Bell, J. B., Lijewski, M. J., Lukić, Z., & Van Andel, E. 2013, <i>ApJ</i>, 765, 39</p> <p>Araya, I. J., & Padilla, N. D. 2014, <i>MNRAS</i>, 445, 850</p> <p>Becker, G. D., Bolton, J. S., Haehnelt, M. G., & Sargent, W. L. W. 2011, <i>MNRAS</i>, 410, 1096</p> | <p>Bolton, J. S., Becker, G. D., Raskutti, S., et al. 2012, <i>MNRAS</i>, 419, 2880</p> <p>Borthakur, S., Heckman, T., Tumlinson, J., et al. 2015, <i>ApJ</i>, 813, 46</p> |
|--|--|

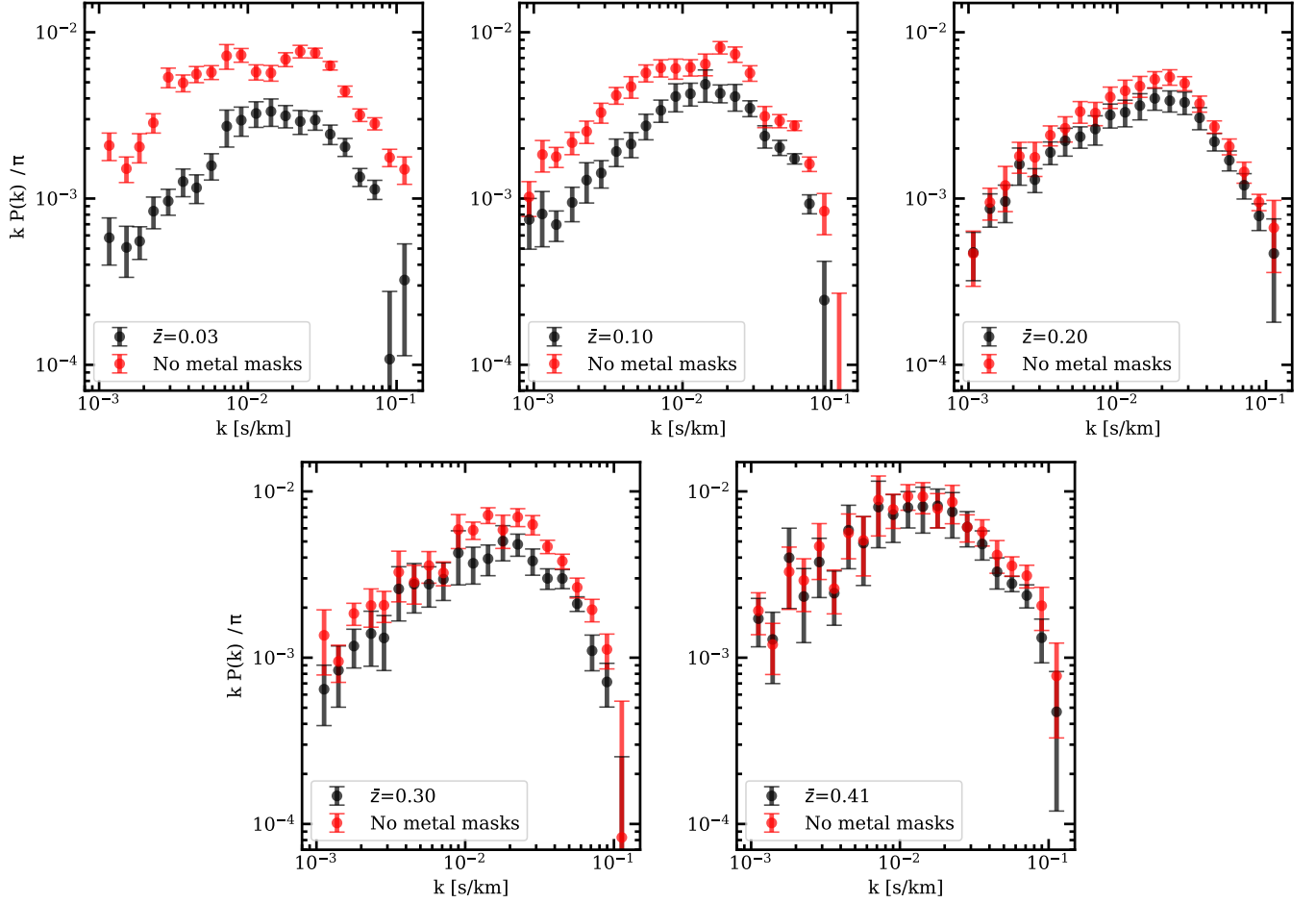


Figure 6. Illustrating the effect of not masking metal absorption (red points). The black points are our power spectrum measurements as shown in Fig. 3. The power without masking metals is systematically higher at all scales. However, the difference in power is larger at lower redshift mostly because of more metal lines from the ISM of the Milky-Way. Note that we are still using the rest wavelength $1050 < \lambda < 1180$ Å; using a wavelength range beyond this will make these deviations even worse.

Burchett, J. N., Tripp, T. M., Prochaska, J. X., et al. 2015, *ApJ*, 815, 91

Croft, R. A. C., Weinberg, D. H., Bolte, M., et al. 2002, *ApJ*, 581, 20

Croft, R. A. C., Weinberg, D. H., Katz, N., & Hernquist, L. 1998, *ApJ*, 495, 44

Danforth, C. W., Keeney, B. A., Tilton, E. M., et al. 2016, *ApJ*, 817, 111

Davé, R., Oppenheimer, B. D., Katz, N., Kollmeier, J. A., & Weinberg, D. H. 2010, *MNRAS*, 408, 2051

Davé, R., & Tripp, T. M. 2001, *ApJ*, 553, 528

Fumagalli, M., Haardt, F., Theuns, T., et al. 2017, *MNRAS*, 467, 4802

Furlanetto, S. R., Oh, S. P., & Pierpaoli, E. 2006, *PhRvD*, 74, 103502

Gaikwad, P., Khaire, V., Choudhury, T. R., & Srianand, R. 2017a, *MNRAS*, 466, 838

Gaikwad, P., Srianand, R., Choudhury, T. R., & Khaire, V. 2017b, *MNRAS*, 467, 3172

Garzilli, A., Boyarsky, A., & Ruchayskiy, O. 2017, *Physics Letters B*, 773, 258

Gunn, J. E., & Peterson, B. A. 1965, *ApJ*, 142, 1633

Gurvich, A., Burkhart, B., & Bird, S. 2017, *ApJ*, 835, 175

Haardt, F., & Madau, P. 2012, *ApJ*, 746, 125

Haehnelt, M. G., & Steinmetz, M. 1998, *MNRAS*, 298, L21

Hiss, H., Walther, M., Hennawi, J. F., et al. 2017, *ArXiv e-prints*, arXiv:1710.00700

Hui, L., & Gnedin, N. Y. 1997, *MNRAS*, 292, 27

Inoue, A. K., Shimizu, I., Iwata, I., & Tanaka, M. 2014, *MNRAS*, 442, 1805

Irsic, V., Viel, M., Haehnelt, M. G., Bolton, J. S., & Becker, G. D. 2017a, *Physical Review Letters*, 119, 031302

Irsic, V., Viel, M., Haehnelt, M. G., et al. 2017b, *Physical Review D*, 96, 023522

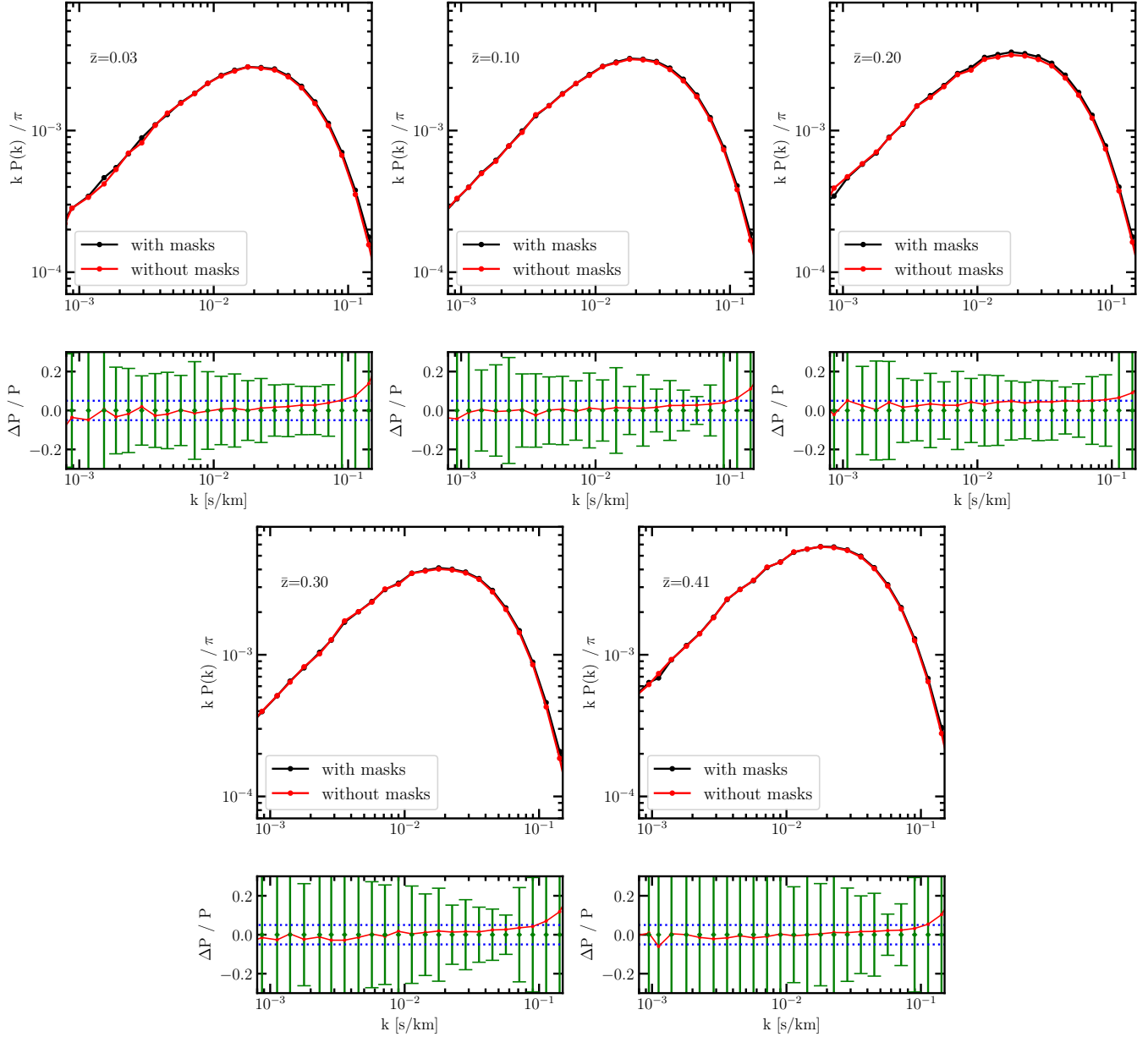


Figure 7. Effect of masking on the power spectrum. We use mock spectra generated from our forward models (infinite signal and resolution) and calculate the power spectrum for two cases. First by applying exactly same masks as in data to the forward model spectra (black-curves) and second where no masks are applied (red curves). The both curves match with each other with $< 5\%$ difference as shown in the bottom panels. The green error-bars show out fractional errors from the measurements. The difference is small enough to ignore and opt-out from doing masking correction.

Khaire, V. 2017, MNRAS, 471, 255

Khaire, V., & Srianand, R. 2015a, MNRAS, 451, L30

—. 2015b, ApJ, 805, 33

—. 2018, ArXiv e-prints, arXiv:1801.09693

Kim, T.-S., Viel, M., Haehnelt, M. G., Carswell, R. F., & Cristiani, S. 2004, MNRAS, 347, 355

Kollmeier, J. A., Weinberg, D. H., Oppenheimer, B. D., et al. 2014, ApJL, 789, L32

Kulkarni, G., Hennawi, J. F., Oñorbe, J., Rorai, A., & Springel, V. 2015, ApJ, 812, 30

Kulkarni, G., Worseck, G., & Hennawi, J. F. 2018, ArXiv e-prints, arXiv:1807.09774

Lamberts, A., Chang, P., Pfrommer, C., et al. 2015, ApJ, 811, 19

Lidz, A., Faucher-Giguère, C.-A., Dall’Aglio, A., et al. 2010, ApJ, 718, 199

Lomb, N. R. 1976, Ap&SS, 39, 447

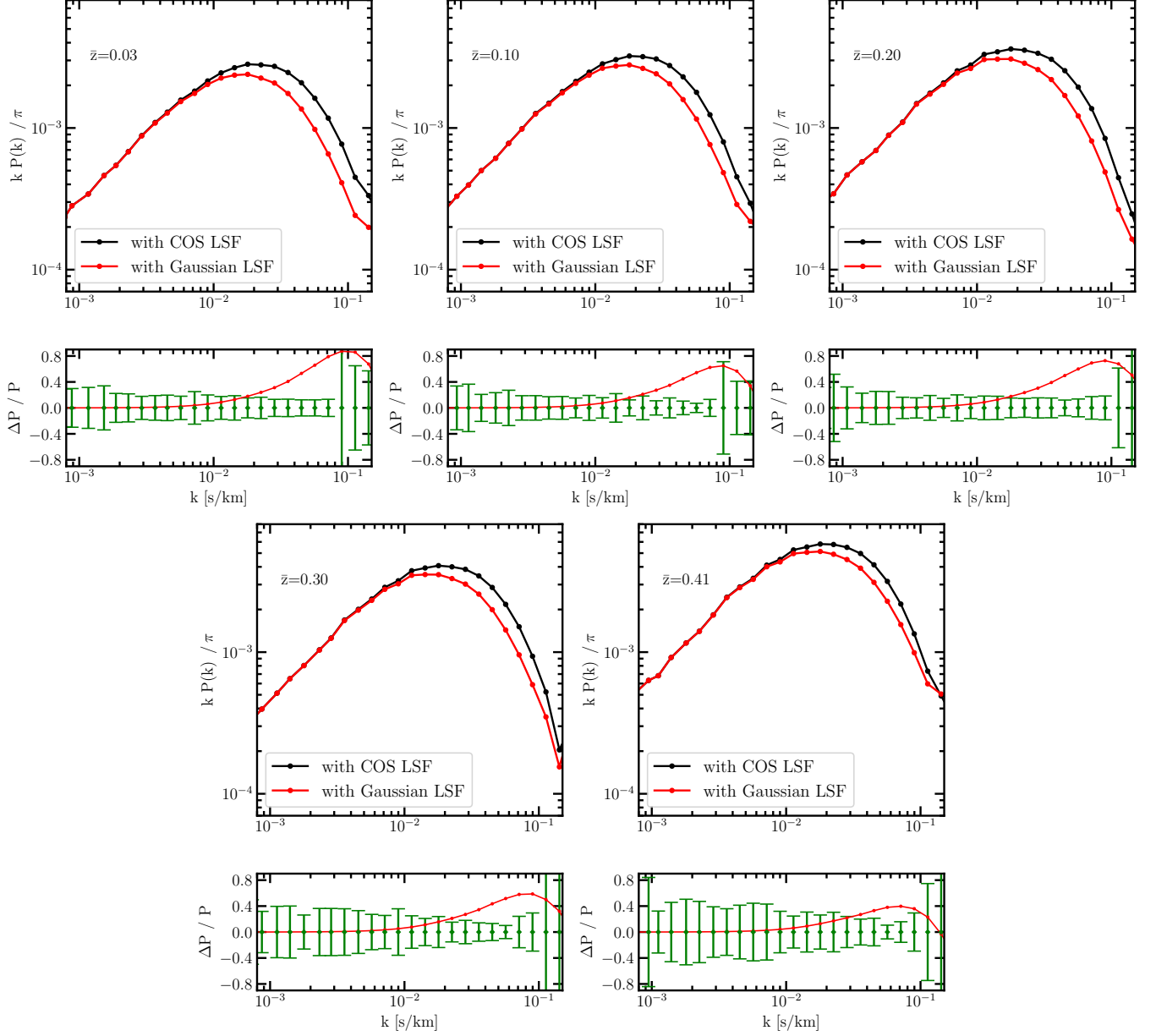


Figure 8. Effect on power spectrum of incorrectly using the Gaussian LSF instead of COS LSF that has broad non-Gaussian wings. We use our forward models generated using the COS LSF and calculate the power spectrum with a Gaussian approximated to COS LSF (red curves). It is compared with the power spectrum calculated using correct COS LSF (black curves). The bottom panels show the percentage difference between these to and compared with the fraction errors estimated from our measurements. The differences are too big to ignore. Therefore, it is never recommended to approximate the COS LSF with a Gaussian, at least for power spectrum calculations.

Lukić, Z., Stark, C. W., Nugent, P., et al. 2015, MNRAS, 446, 3697
 Lusso, E., Worseck, G., Hennawi, J. F., et al. 2015, MNRAS, 449, 4204
 Madau, P., & Dickinson, M. 2014, ARA&A, 52, 415
 Madau, P., & Haardt, F. 2015, ApJL, 813, L8
 McDonald, P., Miralda-Escudé, J., Rauch, M., et al. 2000, ApJ, 543, 1

McDonald, P., Seljak, U., Burles, S., et al. 2006, ApJS, 163, 80
 McQuinn, M. 2016, ARA&A, 54, 313
 Nasir, F., Bolton, J. S., Viel, M., et al. 2017, MNRAS, 471, 1056
 Oñorbe, J., Hennawi, J. F., & Lukić, Z. 2017, ApJ, 837, 106
 Palanque-Delabrouille, N., Yèche, C., Borde, A., et al. 2013, A&A, 559, A85

- Palanque-Delabrouille, N., Yèche, C., Baur, J., et al. 2015, JCAP, 11, 011
- Peebles, M. S., Weinberg, D. H., Davé, R., Fardal, M. A., & Katz, N. 2010, MNRAS, 404, 1281
- Planck Collaboration, Aghanim, N., Akrami, Y., et al. 2018, ArXiv e-prints, arXiv:1807.06209
- Puchwein, E., Haardt, F., Haehnelt, M. G., & Madau, P. 2018, ArXiv e-prints, arXiv:1801.04931
- Puchwein, E., Pfrommer, C., Springel, V., Broderick, A. E., & Chang, P. 2012, MNRAS, 423, 149
- Rahmati, A., Pawlik, A. H., Raicevic, M., & Schaye, J. 2013, MNRAS, 430, 2427
- Ricotti, M., & Shull, J. M. 2000, ApJ, 542, 548
- Rorai, A., Hennawi, J. F., & White, M. 2013, ApJ, 775, 81
- Rorai, A., Hennawi, J. F., Oñorbe, J., et al. 2017, Science, 356, 418
- Scargle, J. D. 1982, ApJ, 263, 835
- Schaye, J., Theuns, T., Leonard, A., & Efstathiou, G. 1999, MNRAS, 310, 57
- Shull, J. M., Harness, A., Trenti, M., & Smith, B. D. 2012, ApJ, 747, 100
- Shull, J. M., Moloney, J., Danforth, C. W., & Tilton, E. M. 2015, ApJ, 811, 3
- Stevans, M. L., Shull, J. M., Danforth, C. W., & Tilton, E. M. 2014, ApJ, 794, 75
- Tepper-García, T. 2006, MNRAS, 369, 2025
- Theuns, T., Leonard, A., Efstathiou, G., Pearce, F. R., & Thomas, P. A. 1998, MNRAS, 301, 478
- Tumlinson, J., Thom, C., Werk, J. K., et al. 2013, ApJ, 777, 59
- Upton Sanderbeck, P. R., D’Aloisio, A., & McQuinn, M. J. 2016, MNRAS, 460, 1885
- Viel, M., Becker, G. D., Bolton, J. S., & Haehnelt, M. G. 2013, PhRvD, 88, 043502
- Viel, M., Becker, G. D., Bolton, J. S., et al. 2008, Physical Review Letters, 100, 041304
- Viel, M., Haehnelt, M. G., Bolton, J. S., et al. 2017, MNRAS, 467, L86
- Wakker, B. P., Hernandez, A. K., French, D. M., et al. 2015, ApJ, 814, 40
- Walther, M., Hennawi, J. F., Hiss, H., et al. 2018a, ApJ, 852, 22
- Walther, M., Oñorbe, J., Hennawi, J. F., & Lukić, Z. 2018b, ArXiv e-prints, arXiv:1808.04367
- Yèche, C., Palanque-Delabrouille, N., Baur, J., & du Mas des Bourboux, H. 2017, JCAP, 6, 047
- Zaldarriaga, M., Hui, L., & Tegmark, M. 2001, ApJ, 557, 519
- Zel’dovich, Y. B. 1970, A&A, 5, 84